THE JOURNAL OF PHYSICAL CHEMISTRY B
A JOURNAL OF THE AMERICAN CHEMICAL SOCIETY

pubs.acs.org/JPCB Article

Stability of Water Confined between Supported Self-Assembled Monolayers

Ramin Mehrani and Sumit Sharma*

Cite This: https://doi.org/10.1021/acs.jpcb.2c00588 Read Online

ACCESS | Metrics & More | Article Recommendations | Supporting Information

ABSTRACT: We present a thermodynamic argument showing that the evaporation and condensation free-energy barriers of water confined between two hydrophobic self-assembled monolayers (SAMs) vary more gradually with the SAM hydrophobicity as compared to the case of water confined between two bare hydrophobic surfaces (no SAMs). We validate our theory by calculating the free-energy profiles of water confined between two SAMs and between two bare surfaces of different hydrophobicities. An implication of our findings is the existence of three regimes of stability of confined water as a function of the hydrophobicity of the SAMs. In comparison to bare planar surfaces with no SAMs, the highly hydrophobic SAMs act to stabilize the liquid state, whereas weakly hydrophobic SAMs stabilize the vapor state of confined water. For intermediate hydrophobicities, the SAMs reduce both the evaporation and the condensation free-energy barriers. These results imply that the effects of SAM hydrophobicity on the behavior of confined water are nontrivial and richer than previously thought.

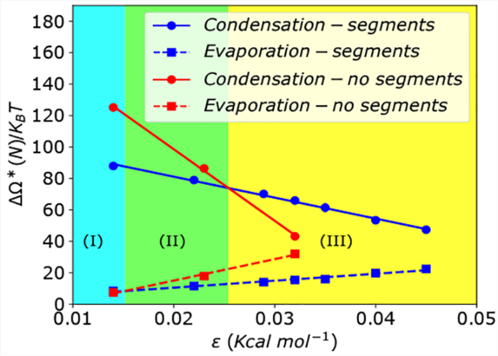

1. INTRODUCTION

Biological self-assembly, including the folding of globular proteins, protein oligomerization, and the formation of lipid bilayers, is understood to be governed by water-mediated interactions. Prior experimental,[1] theoretical,[2,3] and molecular simulation[4−7] studies have shown that liquid water confined between two large (>1 nm) nonpolar solutes becomes metastable below a critical separation, and thus cavitates to the vapor state in equilibrium. Thermodynamic stability of the vapor state is achieved when the enthalpic penalty due to the disruption of the hydrogen bonds of water near large nonpolar solutes exceeds the free-energy cost of creating a vapor−liquid interface between the two solutes.[2,3] Along with the thermodynamical aspect, the kinetics of evaporation of confined water have been deemed to be important in the hydrophobic-effect-driven self-assembly.[7−11] The transition of confined water from the liquid to the vapor phase proceeds via nucleation of a critically sized vapor tube connecting the two solutes.[2,12−14] The nucleation free energy, often termed as the evaporation free-energy barrier, sharply increases with the confinement gap,[13,15,16] thereby significantly slowing down the evaporation rate.[12] The free-energy profile of the formation of a vapor tube in water confined between two parallel and rigid hydrophobic surfaces is well-explained by macroscopic thermodynamics when the contribution of three-phase line tension is incorporated.[16] Interestingly, introducing flexibility in the confining surfaces lowers the evaporation free-energy barrier considerably.[17,18] However, in the case of water confined between two self-assembled monolayers (SAMs), the flexibility of the SAM segments does not affect the evaporation free-energy barrier.[19] In many physical systems of interest, the confining surfaces have protruding moieties, for instance, surfaces with an adsorbed SAM of surfactants, protein interfaces with protruding side chains, corn starch particles with extended polymeric segments, etc.[20−22] These protruding segments are expected to affect the behavior of water confined between the surfaces. Previously, Kanduc and Netz[23] studied the binding propensity in water of two surfaces with SAMs of varying polarity and showed that, for a large range of polarities, the binding is driven by the unfavorable surface water interactions. In this work, we have studied the free-energy behavior of water confined between two surfaces with SAMs of varying hydrophobicity at two different surface densities. We present a thermodynamic argument that the evaporation and the condensation free-energy barriers in the presence of SAMs should vary more gradually as a function of SAM/surface hydrophobicity as compared to the case of bare surfaces. We validate our thermodynamic argument by calculating the evaporation and the condensation free-energy barriers of water confined between two SAMs of varying hydrophobicity as well as between bare surfaces (without SAMs). Our findings highlight three distinct regimes. The first regime, observed for

Received: January 24, 2022
Revised: June 10, 2022

the highly hydrophobic segments, is the one in which the evaporation free-energy barrier is higher but the condensation free-energy barrier is lower in the system with SAMs as compared to the system with bare surfaces. That is, the SAMs stabilize the liquid state. The second regime, observed for intermediate hydrophobicities, is the one in which both the evaporation and the condensation free-energy barriers are lower in the system with the SAMs. In this regime, the SAMs facilitate liquid-to-vapor as well as vapor-to-liquid transitions. The third regime is observed for weakly hydrophobic SAMs. In this regime, the evaporation free-energy barrier is lower but the condensation free-energy barrier is higher for the system with the SAMs. Therefore, in this regime, the presence of the SAMs stabilizes the vapor state of confined water. These findings reveal that the presence of SAMs on surfaces can have important nontrivial effects on the thermodynamic stability of confined water. While the thermodynamic theory explains how the free-energy barriers change with the hydrophobicity of the SAMs as compared to the bare surfaces, the theory is unable to predict the magnitude of the free-energy barriers accurately. It has been shown by Remsing et al.[13] that the evaporation of water confined between hydrophobic surfaces proceeds via a nonclassical pathway wherein vapor bubbles formed close to the hydrophobic surfaces coalesce to form a vapor tube, thereby lowering the evaporation free-energy barriers below the ones predicted by the classical nucleation theory. Nevertheless, as shown previously,[16] growth of the vapor tubes beyond the critical size is well-explained by the macroscopic theory, which explains why the macroscopic theory is still useful in predicting the trends but not the magnitude of the free-energy barriers.

2. SIMULATION SYSTEM AND METHODS

The simulation system comprises two 37.584 Å × 38.50 Å surfaces made up of 896 Lennard-Jones (LJ) atoms arranged in a hexagonal lattice with a lattice constant of 1.4 Å. SAMs are modeled as flexible LJ segments grafted on the surfaces as shown in Figure 1. The two surfaces are placed parallel to each other at a distance $d = 25$ Å. Each segment of the SAMs is made up of three LJ atoms connected via a harmonic bond potential with an equilibrium bond length of 1.4 Å, so the terminal atoms of the segments on the two surfaces are at a distance of 16.6 Å from each other. The segments are flexible, with an angular potential between them with the equilibrium angle of 180°, and are kept perpendicular to the surface via two angular potentials, each with an equilibrium angle of 90°. The surfaces are solvated in water, and the overall size of the simulation system is $70 \times 70 \times 70$ Å^3. The force constants of the bond and the angle potentials are set to 450 kcal/mole·Å^2 and 450 kcal/mole·rad^2, respectively. Our previous work has shown that varying these force constants by as much as 2 orders of magnitude does not affect the free-energy profile of confined water.[19] We have studied systems with SAMs of two different surface densities: 0.1548 and 0.0387 segments/Å, henceforth referred to as the high-density and low-density systems, respectively. Water molecules are modeled using the extended simple point charge model (SPC/E).[24] The surface and the segment atoms interact with the oxygen atom of water molecules (O_w) via the LJ potential. The ϵ parameter of the LJ potential is varied from 0.014 to 0.045 kcal/mol, while the σ parameter is kept fixed at 3.28 Å as in our previous studies.[16,19] For this range of ϵ values, the water contact angle on the bare surfaces varies from 140° to 111°. To compare with real surfaces, the contact angle of water on a lotus leaf is 160°. Silica nanoparticles coated with octadecyl and perylene groups have contact angles in the range of 137−144°.[25] Silanized silica particles have a contact angle of ~130°.[26] Heptadecafluorodecyltrimethoxysilane has a contact angle of 115°. Polytetrafluoroethylene and paraffin have contact angles of 109° and 105°, respectively. The LJ parameters of the surface−O_w interactions are kept the same as those of the segment−O_w interactions. Interactions between the segment atoms and between the segment and the surface atoms are kept at zero. We have also determined free-energy profiles of water confined between two bare surfaces, that is, surfaces with no SAMs. In this system, the two bare surfaces are placed parallel to each other at a distance of 16.6 Å to ensure that the confinement gap in the two systems is the same. We have chosen to perform simulations with the SAMs made up of LJ atoms because this allows us to systematically vary the SAM hydrophobicity via changing the LJ well-depth and compare the results with those obtained for bare surfaces, also made up of LJ atoms of the same hydrophobicity. Furthermore, for the LJ surfaces of different hydrophobicities, we already have good estimates of the water contact angle from our previous work.[16]

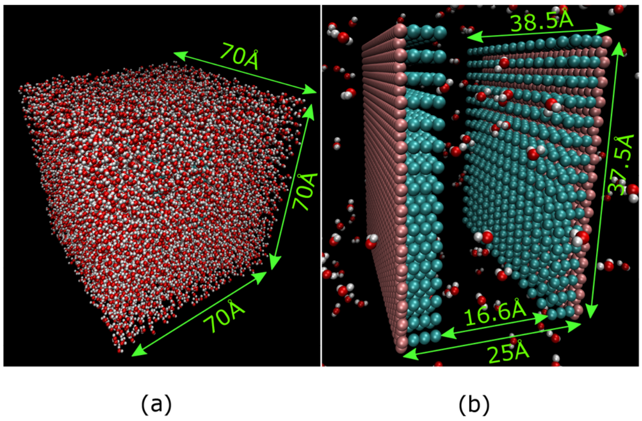

(a) (b)

Figure 1. Snapshots of the simulation system: (a) the simulation box; (b) the two surfaces with SAMs of LJ segments.

2.1. Indirect Umbrella Sampling Simulations.

Free-energy profiles of confined water are determined using the indirect umbrella sampling (INDUS) technique.[27,28] In the INDUS methodology, the density of each atom is smeared in space by modeling it as a truncated Gaussian function. A bias potential, given by $U_{\text{bias}} = \kappa(N - N_0)^2$, is applied, where κ is the force constant, N is the number of water molecules, and N_0 is the target number of water molecules in the confining region. The INDUS parameters are chosen to be the same as in our previous study.[19] κ is set to 0.1 kcal/mol. N_0 is varied from 0 to 650 water molecules in increments of 5 so as to explore the entire range of densities from the liquid to the vapor state. The bias potential is removed to obtain the free-energy profiles using the weighted histogram analysis method (WHAM).[29−32] The simulations are performed in the isothermal−isobaric (NPT) ensemble using the Nose−Hoover thermostat and barostat. Each umbrella sampling window is equilibrated for 1.2 ns, which is followed by a production run of 19.2 ns.

3. RESULTS AND DISCUSSION

3.1. Thermodynamic Relations.

As discussed in the previous works,[3,12,14,16] the evaporation and condensation free-

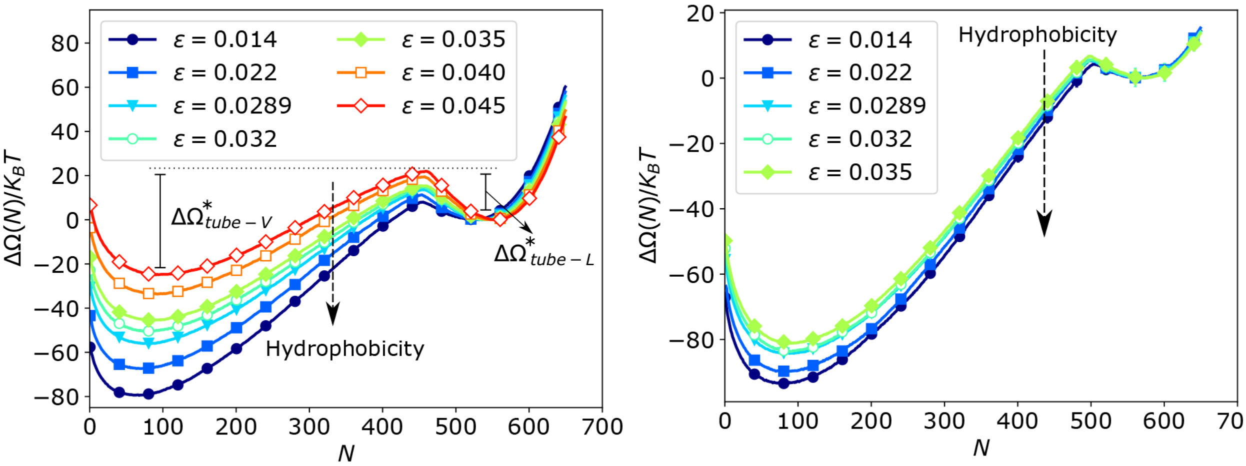

(a) (b)

Figure 2. Free-energy profiles, $\Delta\Omega(N)$, of confined water as a function of the number of molecules, N, for different SAM hydrophobicities, ϵ, and SAM densities of (a) 0.1548 segments/Å and (b) 0.0387 segments/Å. Error bars are standard deviations obtained from seven independent simulations and are smaller than the marker size. ϵ is the well-depth of the LJ interaction potential between the SAM atoms and the water-oxygen atoms.

energy barriers, $\Delta\Omega^*_{\text{tube-L}}$ and $\Delta\Omega^*_{\text{tube-V}}$, respectively, are given by the expressions below (derivation of these expressions is shown in the Supporting Information):

$$\Delta\Omega^*_{\text{tube-L}} = \frac{-\pi(D\gamma_{\text{LV}} + 2\lambda)^2}{2\gamma_{\text{LV}}\cos\theta} \tag{1}$$

$$\Delta\Omega^*_{\text{tube-V}} = -\frac{\pi(D\gamma_{\text{LV}} + 2\lambda)^2}{2\gamma_{\text{LV}}\cos\theta} - 2L^2\gamma_{\text{LV}}\cos\theta - 4L(D\gamma_{\text{LV}} + 2\lambda) \tag{2}$$

where L is the lateral size of the surfaces, D is the confinement gap, γ_{LV} is the liquid-vapor surface tension, and λ is the solid−liquid−vapor line tension.

To estimate the evaporation and the condensation free-energy barriers from these thermodynamic expressions, one needs to know the values of contact angle (θ), the solid−liquid−vapor line tension (λ), and the liquid−vapor surface tension γ_{LV}. γ_{LV} was estimated to be 0.43 N/m for confined water in our previous work.[16] The values of θ and λ for the bare LJ surfaces with different values of ϵ were also obtained in our previous work (Table S1).[16] Figure S1 shows that both $\cos(\theta)$ and $\lambda/\gamma_{\text{LV}}$ vary linearly with ϵ. In the case of surfaces with supported SAMs, one can estimate the contact angle by using the Cassie−Baxter equation[33,34] as follows:

$$\cos\theta_{\text{SAM}} = f_{\text{SAM}}(\cos\theta + 1) - 1 \tag{3}$$

where θ_{SAM} is the contact angle of the droplet on the SAM surface, f_{SAM} is the surface fraction of the SAMs, and θ is the contact angle of the droplet on the bare surface. According to the Cassie−Baxter equation, $\cos\theta_{\text{SAM}} < \cos\theta$, and the contact angle of water on SAM surfaces changes more gradually with ϵ as compared to the bare LJ surfaces.

Table S2 shows the contact angles estimated using the Cassie−Baxter equation for the high-density and low-density SAMs.

For hydrophobic surfaces, $\cos\theta \approx -1$. Let $1 + \cos\theta = x$ so that $x \approx 0$. Equation 1 can now be written as

$$\begin{aligned}\Delta\Omega^*_{\text{tube-L}} &= \frac{\pi(D\gamma_{\text{LV}} + 2\lambda)^2}{2\gamma_{\text{LV}}}[1 + x + O(x^2)] \\ &\approx \frac{\pi(D\gamma_{\text{LV}} + 2\lambda)^2}{2\gamma_{\text{LV}}}(\cos\theta + 2)\end{aligned} \tag{4}$$

Similarly, eq 2 can be written as

$$\begin{aligned}\Delta\Omega^*_{\text{tube-V}} \approx{}& \left[\frac{\pi(D\gamma_{\text{LV}} + 2\lambda)^2}{2\gamma_{\text{LV}}} - 2L^2\gamma_{\text{LV}}\right]\cos\theta \\ &+ \frac{\pi(D\gamma_{\text{LV}} + 2\lambda)^2}{2\gamma_{\text{LV}}} - 4L(D\gamma_{\text{LV}} + 2\lambda)\end{aligned} \tag{5}$$

Therefore, both $\Delta\Omega^*_{\text{tube-L}}$ and $\Delta\Omega^*_{\text{tube-V}}$ should approximately vary linearly with $\cos\theta$. Note that, for the SAM surfaces, we replace θ with θ_{SAM}. For SAM surfaces

$$\frac{\partial\Delta\Omega^*_{\text{tube-L}}}{\partial\epsilon} = \frac{\pi(D\gamma_{\text{LV}} + 2\lambda)^2}{2\gamma_{\text{LV}}} f_{\text{SAM}} \frac{\partial\cos(\theta)}{\partial\epsilon} \tag{6}$$

and

$$\frac{\partial\Delta\Omega^*_{\text{tube-V}}}{\partial\epsilon} = \left[\frac{\pi(D\gamma_{\text{LV}} + 2\lambda)^2}{2\gamma_{\text{LV}}} - 2L^2\gamma_{\text{LV}}\right] f_{\text{SAM}} \frac{\partial\cos(\theta)}{\partial\epsilon} \tag{7}$$

The equations corresponding to eqs 6 and 7 for the case of bare surfaces can be obtained by simply substituting $f_{\text{SAM}} = 1$. For the bare LJ surfaces, the line tension terms are needed to match the thermodynamic theory to the simulation results.[16] However, in the case of SAMs, the role of line tension is debatable as there is no clearly defined three-phase contact line. If, for the case of SAMs, we ignore the line tension terms in the above equations, then both $\Delta\Omega^*_{\text{tube-L}}$ and $\Delta\Omega^*_{\text{tube-V}}$ are expected to vary linearly with ϵ. Equations 6 and 7 imply that we should expect $\Delta\Omega^*_{\text{tube-L}}$ and $\Delta\Omega^*_{\text{tube-V}}$ for the SAM surfaces to vary more gradually as a function of ϵ in comparison to the case of bare LJ surfaces. We test these thermodynamic arguments via molecular simulations.

https://doi.org/10.1021/acs.jpcb.2c00588

3.2. Free-Energy Profiles. Parts a and b of Figure 2 show the free-energy profiles of confined water in the high-density and the low-density systems, respectively, as a function of ϵ. With an increase in the value of ϵ, that is, decreasing hydrophobicity, the evaporation free-energy barrier increases and the condensation free-energy barrier decreases, implying that the liquid phase becomes more stable and the vapor phase becomes less stable. It is observed that, with the increase in the value of ϵ, the decrease in the stability of the vapor phase is more rapid as compared to the increase in the stability of the liquid phase for both the high-density and low-density systems. This result is explained by eqs 6 and 7, according to which the magnitude of the slope of $\Delta\Omega^{*}_{\text{tube-V}}$ as a function of ϵ or, equivalently, $\cos(\theta)$ is larger than that of $\Delta\Omega^{*}_{\text{tube-L}}$. Figure 3 shows the free-energy profiles of water confined between bare surfaces as a function of ϵ. The free-energy profiles show a similar trend, but the evaporation and the condensation free-energy barriers change more dramatically as a function of ϵ compared to the case of the surfaces with the SAMs. This result also aligns with the predictions of our thermodynamic theory (eqs 6 and 7). Furthermore, using eqs 6 and 7, from the rate of change of the evaporation and the condensation free-energy barriers with $\cos(\theta)$ one can get an estimate of γ_{LV}. Figure S2 shows the evaporation and the condensation free-energy barriers as a function of $\cos(\theta)$ for the high-density SAMs, low-density SAMs, and bare surfaces. From the results of the high-density SAMs and the bare surfaces, γ_{LV} is estimated to be 0.062 and 0.056 N/m, respectively, which is in close agreement with the γ_{LV} of SPC/E water. In the case of low-density SAMs, the variation in $\cos(\theta)$ is small, and as a result, the estimate of the slopes is erroneous.

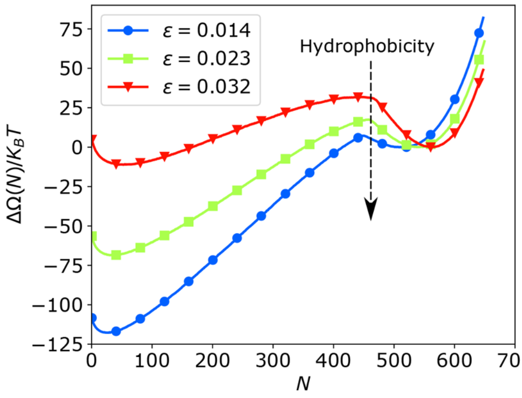

Figure 3. Free-energy profiles, $\Delta\Omega(N)$, of confined water as a function of the number of molecules, N, for the system with bare surfaces as a function of ϵ. Error bars are standard deviations obtained from seven independent simulations and are smaller than the marker size. ϵ is the well-depth of LJ interaction potential between the surface atoms and water-oxygen atoms.

Parts a and b of Figure 4 compare the evaporation and the condensation free-energy barriers estimated from the thermodynamic theory (eqs 1 and 2) with the simulation results for the case of bare LJ surfaces. The predictions of the theory show some mismatch with the simulation results. Specifically, the evaporation free-energy barriers predicted from the theory are higher than those obtained in our simulations presumably due to the nonclassical evaporation pathways wherein isolated vapor bubbles close to the surfaces coalesce to form a gap-spanning vapor tube.[13]

Parts a and b of Figure 5 show the evaporation and the condensation free-energy barriers for the SAMs and for the bare surfaces as a function of ϵ. As predicted from the thermodynamic theory, the free-energy barriers in the case of the SAMs change more gradually with ϵ compared to those of bare surfaces. According to the theory, the ratio of the slopes of evaporation and condensation free-energy barriers versus ϵ for the cases of SAMs and bare surfaces should be equal to f_{SAM} (eqs 6 and 7). For the high-density SAMs, the calculated f_{SAM} is 0.28 (Figure S3). The ratio of the slopes of the condensation free-energy barriers versus ϵ for the high-density SAMs and bare surface is found to be 0.29 and that for the evaporation free-energy barriers is found to be 0.32. Similarly, for the low-density SAMs, f_{SAM} is 0.065 and the ratios of the slopes for the condensation and the evaporation free-energy barriers versus ϵ are 0.1 and 0.072, respectively. Therefore, the thermodynamic theory provides a reasonably good explanation for the differences in the rate of change of the evaporation and the condensation free-energy barriers with ϵ because of the influence of the SAMs. From the simulation results, we identify three different regimes (Figure 5, parts a and b): in regime I, observed for the highly hydrophobic surfaces/SAMs, the evaporation free-energy barrier is higher and the condensation free-energy barrier is lower for the surfaces with SAMs. So, in regime I the liquid phase is stabilized by the

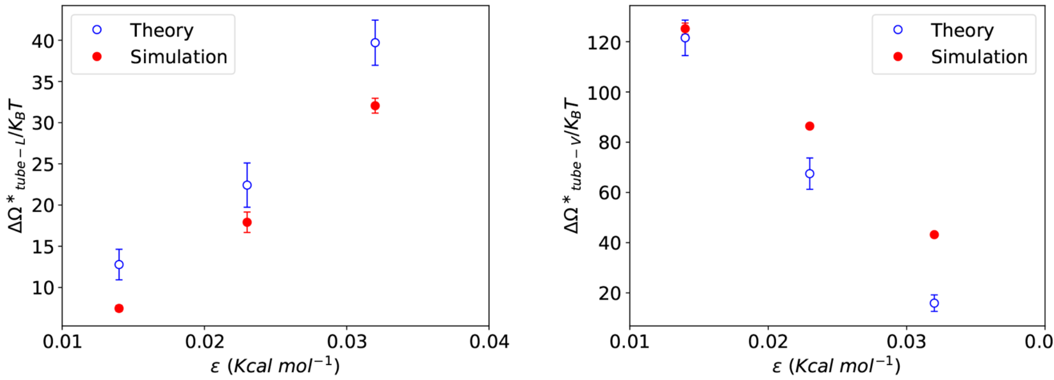

(a) (b)

Figure 4. Comparison between the (a) evaporation and (b) condensation free-energy barrier calculated from the macroscopic theory with the simulation results for the bare surfaces as a function of LJ well-depth parameter ϵ.

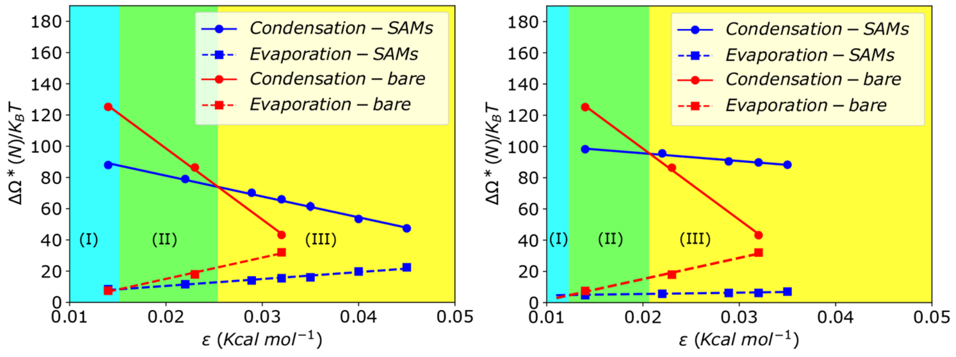

(a) (b)

Figure 5. Condensation and the evaporation free-energy barriers as a function of the LJ well-depth parameter ϵ for the (a) high-density and the (b) low-density SAM systems. Lines are added as guides to the eye. Solid lines show the condensation free-energy barrier, and dashed lines show the evaporation free-energy barrier. Blue- and red-colored lines represent the system with surfaces with and without the SAMs, respectively.

SAMs. The second regime (II) is observed for intermediate hydrophobicities wherein both the evaporation and the condensation free-energy barriers are lower for the surfaces with SAMs. Therefore, in regime II, the presence of the SAMs facilitates liquid-to-vapor as well as vapor-to-liquid transitions in confined water. Lastly, regime III is observed in the case of weakly hydrophobic surfaces/SAMs. In regime III, the evaporation free-energy barrier is lower but the condensation free-energy barrier is higher for the SAMs. So, in regime III, it is the vapor phase that is stabilized by the SAMs. It is clear from Figure 5, parts a and b, that regime III spans the largest range of ϵ.

We have also calculated the average lateral compressive/tensile forces acting on the confining surfaces as a function of ϵ for the case of bare surfaces and for the SAMs (Figure 6).

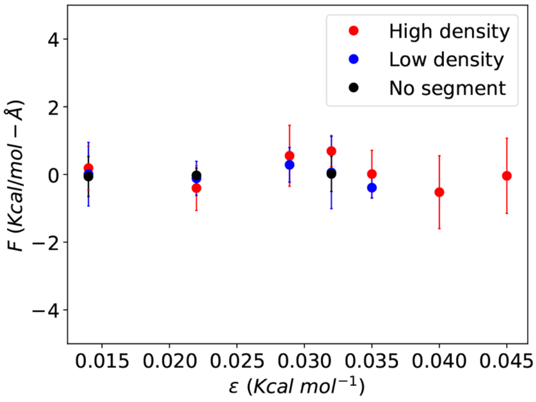

Figure 6. Average lateral forces acting on the surfaces as a function of ϵ. Error bars are standard deviations calculated from four independent simulations.

These lateral forces are responsible for the hydrophobic collapse of the surfaces. Interestingly, no differences in the average lateral forces are observed in the three cases, suggesting that, at the studied confinement gap, the SAMs do not have any effect on the lateral forces acting on the surfaces. Figure S4 shows the density of water confined between the two surfaces with (Figure S4a) high-density SAMs, (Figure S4b) low-density SAMs, and (Figure S4c) no SAMs. In the case of the bare surfaces, significant attenuation in the layering of confined water is observed when ϵ is decreased from 0.032 kcal/mol, whereas the surfaces with the SAMs do not show much layering of confined water. Figures S5 and S6 show the evaporation and the condensation free-energy barriers predicted by the macroscopic thermodynamic theory (excluding the line tension terms) and the results obtained from the simulations of the high- and low-density SAMs, respectively. It is observed that the magnitudes of the barriers predicted from the macroscopic theory in the case of the SAMs deviate from the simulation results. Therefore, while the thermodynamic theory is able to explain the change in the free-energy barriers with ϵ, it is unable to match the magnitude of these barriers. Even when the effect of line tension is ignored in the theory, the theory still fails to match the magnitude of the free-energy barriers obtained in the simulations (Figures S7 and S8). As discussed before, the breakdown of classical nucleation theory in explaining the magnitudes of the free-energy barriers is presumably due to the nonclassical pathways associated with the formation of the vapor tube in the confined region.[13]

4. CONCLUSIONS

In this work we present a macroscopic thermodynamics theory that predicts the role of hydrophobic SAMs on the evaporation and condensation free-energy barriers of confined water. The theory is able to predict quite well how the free-energy barriers are expected to change with the change in the hydrophobicity of the SAMs. The simulation results show that, for superhydrophobic surfaces, the presence of SAMs on the confining surfaces acts to reduce the hydrophobicity. At the other end of the spectrum, for weakly hydrophobic surfaces, the presence of SAMs enhances the surface hydrophobicity. Furthermore, it is observed that, for the low-density SAM system, regimes I and II are shifted toward smaller values of ϵ as compared to the high-density system. Therefore, for the low-density system there is a larger range of hydrophobicities for which the SAMs act to enhance the surface hydrophobicity. While the thermodynamic theory explains how the free-energy barriers change with the polarity of the SAMs as compared to the bare surfaces, the theory is unable to predict the magnitude of the free-energy barriers accurately. The breakdown of the macroscopic theory in explaining the magnitudes of the computed free-energy barriers is probably due to the nonclassical pathways that are associated with the formation of vapor tubes in the confined region.

■ ASSOCIATED CONTENT

Supporting Information

The Supporting Information is available free of charge at https://pubs.acs.org/doi/10.1021/acs.jpcb.2c00588.

> Derivation of eqs 1 and 2, table of thermodynamic properties required for the estimation of evaporation and condensation free-energy barriers from thermodynamic expressions for SAMs and bare hydrophobic surfaces, variation of thermodynamic properties as a function of ϵ for the case of a bare surface, comparison between the variation of condensation and evaporation free-energy barriers as a function of the cosine of contact angle for SAMs and bare hydrophobic surfaces, comparison of the changes in contact angle with respect to the hydrophobicity of surfaces between all cases of SAMs and bare surfaces, water density plot for SAMs and bare hydrophobic surfaces, and comparison between the macroscopic theory and simulation results for SAMs by considering the line tension effect in the theory and the absence of the line tension effect in the theory (PDF)

■ AUTHOR INFORMATION

Corresponding Author

Sumit Sharma – *Department of Chemical and Biomolecular Engineering, Ohio University, Athens, Ohio 45701, United States*; orcid.org/0000-0003-3138-5487; Email: sharmas@ohio.edu

Author

Ramin Mehrani – *Department of Mechanical Engineering, Ohio University, Athens, Ohio 45701, United States*

Complete contact information is available at: https://pubs.acs.org/10.1021/acs.jpcb.2c00588

Notes

The authors declare no competing financial interest.

■ ACKNOWLEDGMENTS

This work is supported by the NSF CDS&E Grant 1953311 and NSF CAREER Grant 2046095. Computational resources for this work were provided by the Ohio Supercomputer Center and National Science Foundation XSEDE Grant No. DMR190005.

■ REFERENCES

(1) Christenson, H. K.; Claesson, P. M. Cavitation and the interaction between macroscopic hydrophobic surfaces. *Science* **1988**, *239*, 390−392.

(2) Lum, K.; Chandler, D.; Weeks, J. D. Hydrophobicity at Small and Large Length Scales. *J. Phys. Chem. B* **1999**, *103*, 4570−4577.

(3) Cerdeiriña, C. A.; Debenedetti, P. G.; Rossky, P. J.; Giovambattista, N. Evaporation Length Scales of Confined Water and Some Common Organic Liquids. *J. Phys. Chem. Lett.* **2011**, *2*, 1000−1003.

(4) Leung, K.; Luzar, A.; Bratko, D. Dynamics of capillary drying in water. *Phys. Rev. Lett.* **2003**, *90*, 065502.

(5) Huang, X.; Zhou, R.; Berne, B. J. Drying and hydrophobic collapse of paraffin plates. *J. Phys. Chem. B* **2005**, *109*, 3546−3552.

(6) Choudhury, N.; Pettitt, B. M. On the mechanism of hydrophobic association of nanoscopic solutes. *J. Am. Chem. Soc.* **2005**, *127*, 3556−3567.

(7) Zhou, R.; Huang, X.; Margulis, C. J.; Berne, B. J. Hydrophobic collapse in multidomain protein folding. *Science* **2004**, *305*, 1605−1609.

(8) TenWolde, P. R.; Chandler, D. Drying-induced hydrophobic polymer collapse. *Proc. Natl. Acad. Sci. U. S. A.* **2002**, *99*, 6539−6543.

(9) Huang, X.; El-Sayed, I. H.; Qian, W.; El-Sayed, M. A. Cancer cell imaging and photothermal therapy in the near-infrared region by using gold nanorods. *J. Am. Chem. Soc.* **2006**, *128*, 2115−2120.

(10) Wang, Y.; DePrince, A. E., III; Gray, S. K.; Lin, X.-M.; Pelton, M. Solvent-mediated end-to-end assembly of gold nanorods. *journal of physical chemistry letters* **2010**, *1*, 2692−2698.

(11) Comtet, J.; Chatté, G.; Niguès, A.; Bocquet, L.; Siria, A.; Colin, A. Pairwise Frictional Profile Between Particles Determines Discontinuous Shear Thickening Transition in Non-Colloidal Suspensions. *Nat. Commun.* **2017**, *8*, 15633.

(12) Sharma, S.; Debenedetti, P. G. Evaporation Rate of Water in Hydrophobic Confinement. *Proc. Natl. Acad. Sci. U. S. A.* **2012**, *109*, 4365−4370.

(13) Remsing, R. C.; Xi, E.; Vembanur, S.; Sharma, S.; Debenedetti, P. G.; Garde, S.; Patel, A. J. Pathways to Dewetting in Hydrophobic Confinement. *Proc. Natl. Acad. Sci. U. S. A.* **2015**, *112*, 8181−8186.

(14) Luzar, A. Activation barrier scaling for the spontaneous evaporation of confined water. *J. Phys. Chem. B* **2004**, *108*, 19859−19866.

(15) Sharma, S.; Debenedetti, P. G. Free Energy Barriers to Evaporation of Water in Hydrophobic Confinement. *J. Phys. Chem. B* **2012**, *116*, 13282−13289.

(16) Ghasemi, M.; Ramsheh, S. M.; Sharma, S. Quantitative Assessment of Thermodynamic Theory in Elucidating the Behavior of Water Under Hydrophobic Confinement. *J. Phys. Chem. B* **2018**, *122*, 12087−12096.

(17) Altabet, Y. E.; Debenedetti, P. G. The Role of Material Flexibility on the Drying Transition of Water Between Hydrophobic Objects: A Thermodynamic Analysis. *J. Chem. Phys.* **2014**, *141*, 18C531.

(18) Altabet, Y. E.; Haji-Akbari, A.; Debenedetti, P. G. Effect of Material Flexibility on the Thermodynamics and Kinetics of Hydrophobically Induced Evaporation of Water. *Proc. Natl. Acad. Sci. U. S. A.* **2017**, *114*, E2548−E2555.

(19) Mehrani, R.; Sharma, S. Behavior of water confined between hydrophobic surfaces with grafted segments. *Colloid and Interface Science Communications* **2021**, *40*, 100355.

(20) Chou, K.-C.; Zhang, C.-T.; Maggiora, G. M. Disposition of amphiphilic helices in heteropolar environments. *Proteins: Struct., Funct., Bioinf.* **1997**, *28*, 99−108.

(21) Clackson, T.; Wells, J. A. A hot spot of binding energy in a hormone-receptor interface. *Science* **1995**, *267*, 383−386.

(22) Eyrisch, S.; Helms, V. Transient pockets on protein surfaces involved in protein- protein interaction. *Journal of medicinal chemistry* **2007**, *50*, 3457−3464.

(23) Kanduč, M.; Netz, R. R. From hydration repulsion to dry adhesion between asymmetric hydrophilic and hydrophobic surfaces. *Proc. Natl. Acad. Sci. U. S. A.* **2015**, *112*, 12338−12343.

(24) Berendsen, H.; Grigera, J.; Straatsma, T. The Missing Term in Effective Pair Potentials. *J. Phys. Chem.* **1987**, *91*, 6269−6271.

(25) Sriramulu, D.; Reed, E. L.; Annamalai, M.; Venkatesan, T. V.; Valiyaveettil, S. Synthesis and characterization of superhydrophobic, self-cleaning NIR-reflective silica nanoparticles. *Sci. Rep.* **2016**, *6*, 35993.

(26) Tsai, P.-S.; Yang, Y.-M.; Lee, Y.-L. Fabrication of hydrophobic surfaces by coupling of langmuir- blodgett deposition and a self-assembled monolayer. *Langmuir* **2006**, *22*, 5660−5665.

(27) Patel, A. J.; Varilly, P.; Chandler, D. Fluctuations of Water Near Extended Hydrophobic and Hydrophilic Surfaces. *J. Phys. Chem. B* **2010**, *114*, 1632−1637.

(28) Patel, A. J.; Varilly, P.; Chandler, D.; Garde, S. Quantifying Density Fluctuations in Volumes of All Shapes and Sizes Using Indirect Umbrella Sampling. *Journal of statistical physics* **2011**, *145*, 265−275.

(29) Grossfield, A. *WHAM: The Weighted Histogram Analysis Method*, ver. 2.0.9.; http://membrane.urmc.rochester.edu/wordpress/?page_id=126.

(30) Kästner, J. Umbrella sampling. *WIREs Comput. Mol. Sci.* **2011**, *1*, 932−942.

(31) Kumar, S.; Rosenberg, J. M.; Bouzida, D.; Swendsen, R. H.; Kollman, P. A. The Weighted Histogram Analysis Method for Free-Energy Calculations on Biomolecules. I. The Method. *Journal of computational chemistry* **1992**, *13*, 1011−1021.

(32) Souaille, M.; Roux, B. Extension to the Weighted Histogram Analysis Method: Combining Umbrella Sampling with Free Energy Calculations. *Computer physics communications* **2001**, *135*, 40−57.

(33) Cassie, A.; Baxter, S. Wettability of porous surfaces. *Trans. Faraday Soc.* **1944**, *40*, 546−551.

(34) Daub, C. D.; Wang, J.; Kudesia, S.; Bratko, D.; Luzar, A. The influence of molecular-scale roughness on the surface spreading of an aqueous nanodrop. *Faraday Discuss.* **2010**, *146*, 67−77.